Cell Reports

Structural basis for translation inhibition by MERS-CoV Nsp1 reveals a conserved mechanism for betacoronaviruses

Graphical abstract

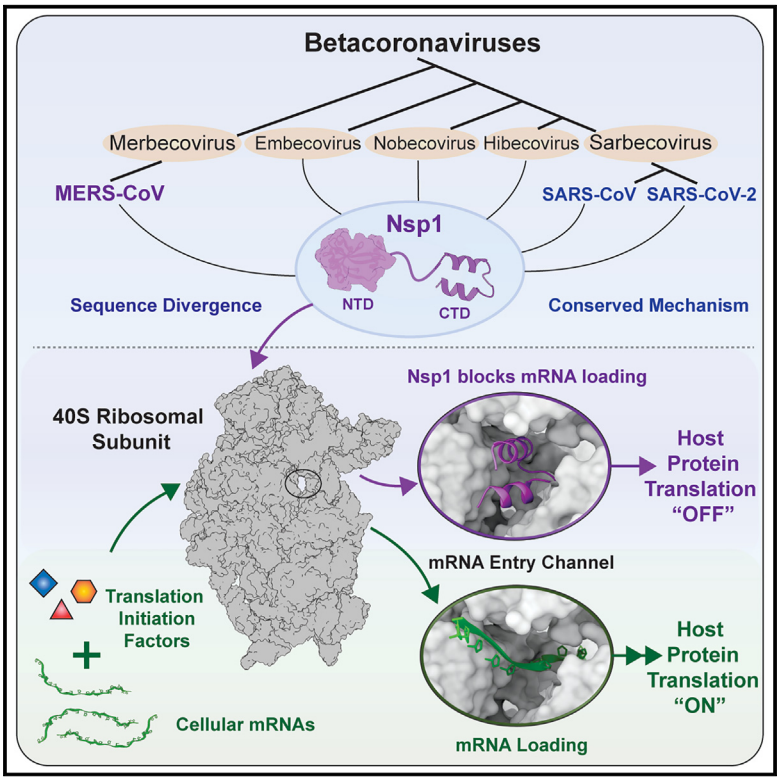

Highlights

- MERS-CoV Nsp1 directly interacts with the human 40S ribosome and inhibits translation
- The CTD of MERS-CoV Nsp1 sterically blocks the mRNA entry channel of the 40S ribosome
- CTD of MERS-CoV Nsp1 is indispensable for its translation inhibition activity
- Evolutionarily divergent SARS-CoV-2 and MERS-CoV Nsp1 share a remarkably conserved mechanism

Authors

Swapnil C. Devarkar, Michael Vetick, Shravani Balaji, ..., Wendy V. Gilbert, Sidi Chen, Yong Xiong

Correspondence

yong.xiong@yale.edu

In brief

Devarkar and Vetick et al. present a high-resolution cryo-EM structure of the human 40S ribosome-MERS-CoV Nsp1 complex. MERS-CoV Nsp1 inhibits translation by blocking the mRNA entry channel with its C-terminal domain. The study reveals a remarkably conserved mechanism for Nsp1 across evolutionarily divergent betacoronaviruses.

Devarkar et al., 2023, Cell Reports *42*, 113156
October 31, 2023
https://doi.org/10.1016/j.celrep.2023.113156

CellPress

Cell Reports

CellPress
OPEN ACCESS

Report

Structural basis for translation inhibition by MERS-CoV Nsp1 reveals a conserved mechanism for betacoronaviruses

Swapnil C. Devarkar,[1,5] Michael Vetick,[1,5] Shravani Balaji,[1] Ivan B. Lomakin,[2] Luojia Yang,[3,4] Danni Jin,[1] Wendy V. Gilbert,[1] Sidi Chen,[3,4] and Yong Xiong[1,6,*]

[1]Department of Molecular Biophysics and Biochemistry, Yale University, New Haven, CT 06511, USA
[2]Department of Dermatology, Yale University School of Medicine, New Haven, CT 06520, USA
[3]Systems Biology Institute, Yale University, West Haven, CT 06516, USA
[4]Department of Genetics, Yale University School of Medicine, New Haven, CT 06520, USA
[5]These authors contributed equally
[6]Lead contact
*Correspondence: yong.xiong@yale.edu
https://doi.org/10.1016/j.celrep.2023.113156

SUMMARY

All betacoronaviruses (β-CoVs) encode non-structural protein 1 (Nsp1), an essential pathogenicity factor that potently restricts host gene expression. Among the β-CoV family, MERS-CoV is the most distantly related member to SARS-CoV-2, and the mechanism for host translation inhibition by MERS-CoV Nsp1 remains controversial. Herein, we show that MERS-CoV Nsp1 directly interacts with the 40S ribosomal subunit. Using cryogenic electron microscopy (cryo-EM), we report a 2.6-Å structure of the MERS-CoV Nsp1 bound to the human 40S ribosomal subunit. The extensive interactions between C-terminal domain of MERS-CoV Nsp1 and the mRNA entry channel of the 40S ribosomal subunit are critical for its translation inhibition function. This mechanism of MERS-CoV Nsp1 is strikingly similar to SARS-CoV and SARS-CoV-2 Nsp1, despite modest sequence conservation. Our results reveal that the mechanism of host translation inhibition is conserved across β-CoVs and highlight a potential therapeutic target for the development of antivirals that broadly restrict β-CoVs.

INTRODUCTION

Since 2002, three human betacoronaviruses (β-CoVs) have emerged causing severe respiratory syndromes: severe acute respiratory syndrome-CoV (SARS-CoV),[1] Middle East respiratory syndrome-CoV (MERS-CoV),[2] and severe acute respiratory syndrome-CoV-2 (SARS-CoV-2), the cause of the COVID-19 pandemic.[3] Nsp1 is an essential virulence factor that restricts host gene expression post-transcriptionally and has been shown to specifically inhibit the expression of interferon-stimulated genes to abrogate the innate immune response.[4–6] While Nsp1 is encoded by all β-CoVs, it is notable that there is a large divergence in its primary amino acid sequence.[7] SARS-CoV and SARS-CoV-2 Nsp1 share a high degree of protein sequence identity (88%), but MERS-CoV Nsp1 is poorly conserved, only sharing 13%–16% sequence identity with Nsp1 from other mammalian β-CoVs[8] (Figure S1A). Despite the lack of sequence conservation, β-CoV Nsp1 proteins are predicted to share a similar architecture to the reported structures of SARS-CoV[9] and SARS-CoV-2 Nsp1,[10,11] with a beta-barrel N-terminal domain (NTD) and a short C-terminal domain (CTD), separated by a flexible linker region[5,12–14] (Figure S1B).

While structural predictions for Nsp1 from different β-CoV species show similar global structure, these proteins are reported to have significant differences in protein function, particularly for MERS-CoV Nsp1. Currently, there are three distinct mechanisms of host gene expression inhibition proposed for β-CoV Nsp1: two cytosolic and one nuclear.[7] In the cytosol, the CTD of Nsp1 binds the mRNA entry channel of the 40S ribosomal subunit, sterically inhibiting host mRNA from being properly loaded during translation initiation.[5,13,15] Also, in a ribosome-dependent manner, Nsp1 coordinates endonuclease cleavage of the 5′ end of host transcripts, restricting their expression and promoting their degradation by cellular exonucleases.[16,17] Lastly, within the nucleus, Nsp1 is believed to bind and inhibit the host mRNA nuclear transport complex NXF1/NXT1, which impedes host mRNA transport.[18] While several studies have shown that SARS-CoV and SARS-CoV-2 Nsp1 likely employ all these mechanisms,[5,16,18,19] how MERS-CoV Nsp1 inhibits host protein synthesis remains controversial.[20,21] The current literature on MERS-CoV Nsp1 suggests that its role is restricted to the nucleus and that it does not directly bind to the 40S ribosomal subunit.[20]

Herein, using a combination of biochemical and structural methods, we show that MERS-CoV Nsp1 binds the 40S ribosomal subunit and inhibits protein translation in *in vitro* translation assays. We report a 2.6-Å cryo-EM structure of the MERS-CoV Nsp1 in complex with the human 40S ribosomal subunit

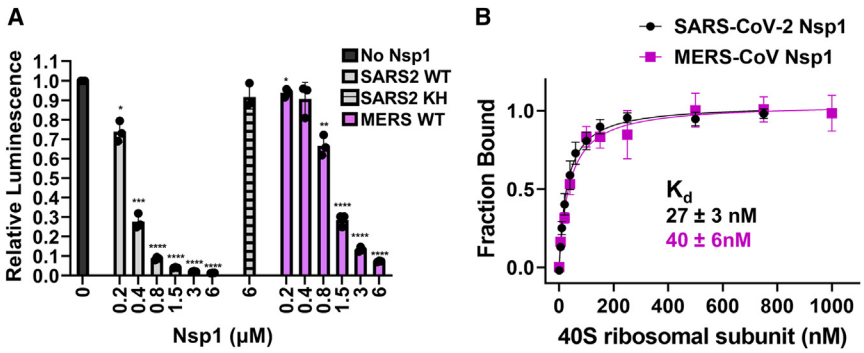

Figure 1. MERS-CoV Nsp1 binds 40S ribosome and inhibits protein translation

(A) *In vitro* protein translation of a luciferase mRNA in the presence of WT SARS-CoV-2, K164A/H165A SARS-CoV-2 Nsp1, and WT MERS-CoV Nsp1. Data are the mean of three biological replicates +/− one standard deviation. Each biological replicate is the average of three technical replicates. Values for Nsp1-containing reactions were compared to the "No Nsp1" control using two-tailed, unpaired Student's t tests. *p < 0.05, **p < 0.01, ***p < 0.001, ****p < 0.0001.

(B) Fluorescence polarization-based binding affinity titrations of 40S ribosome against fluorescein-tagged SARS-CoV-2 or MERS-CoV Nsp1. The titrations were done in triplicates, and the average value for each titration point with the associated standard deviation is shown. The curves were fit to a one-site binding equation, and the estimated K_d and the associated standard deviation are shown. Also refer to Figure S1.

that reveals the molecular basis for host translation inhibition by MERS-CoV Nsp1. MERS-CoV Nsp1 CTD engages the mRNA entry channel of the 40S ribosomal subunit in a similar fashion to SARS-CoV-2 Nsp1, despite only modest sequence conservation. Our structure also confirms previous bioinformatics analyses predicting that the Nsp1 CTD of even divergent betacoronaviruses shares a conserved "helix-turn-helix" fold.[8,14] This interaction with the 40S ribosomal subunit is critical for the translation inhibition function of MERS-CoV Nsp1. Our results show that even divergent species of β-CoVs employ a remarkably similar mechanism for host translation inhibition, presenting an attractive potential target for development of novel therapeutics broadly restricting β-CoV species.

RESULTS

MERS-CoV Nsp1 binds 40S ribosome and inhibits protein translation

Previous studies propose that unlike SARS-CoV and SARS-CoV-2 Nsp1, MERS-CoV Nsp1 does not inhibit translation through interactions with the ribosome, but rather, its mode of action is restricted to the nucleus.[7,20] To test this hypothesis, we carried out a comparative analysis of purified SARS-CoV-2 and MERS-CoV Nsp1 proteins for their ability to inhibit translation of a luciferase reporter mRNA in an *in vitro* translation system of HeLa cell lysate. Wild-type (WT) SARS-CoV-2 Nsp1 exhibited strong translation inhibition with a comparable dose response to prior published studies[19,22] (Figure 1A). Also as previously reported, mutation of key residues K164A/H165A in SARS-CoV-2 Nsp1, which interact with the 18S rRNA of the ribosome, abolished the translation inhibition activity.[19,23,24] Surprisingly, MERS-CoV Nsp1 showed robust inhibition of the luciferase mRNA translation, contrary to predictions based on current literature.[24] Compared to MERS-CoV Nsp1, SARS-CoV-2 Nsp1 exhibits a stronger dose-response behavior, suggesting SARS-CoV-2 Nsp1 inhibits translation more efficiently (Figure 1A).

Based on this result, we tested SARS-CoV-2 and MERS-CoV Nsp1 for direct binding to purified 40S ribosomal subunits using ultracentrifugation through a 30% sucrose cushion. Both proteins co-migrated with the 40S ribosomal subunit, indicating that MERS-CoV Nsp1 can directly interact with the 40S ribosomal subunit (Figure S1C), contrary to previously proposed models.[20] We next used fluorescence polarization-based binding assays to quantitatively characterize the binding of MERS-CoV and SARS-CoV-2 Nsp1 to the 40S ribosomal subunit. For this assay, MERS-CoV and SARS-CoV-2 Nsp1 were mutated to have a single solvent-exposed cysteine residue, which enabled labeling by a single fluorescein group through maleimide-thiol conjugation. The modified versions of MERS-CoV and SARS-CoV-2 Nsp1 (Cys MERS and Cys SARS2, respectively) were assayed for their activity by *in vitro* translation assays. Cys MERS and Cys SARS2 showed comparable levels of translational inhibition to their WT counterparts, indicating that the mutagenesis did not significantly affect protein folding or activity (Figure S1D). Fluorescence polarization-based titrations showed that MERS-CoV Nsp1 binds the 40S ribosomal subunit with an affinity of ~40 nM, whereas SARS-CoV-2 Nsp1 binding affinity for the 40S ribosomal subunit is ~27 nM (Figure 1B).

Cryo-EM structure of MERS-CoV Nsp1 bound to human 40S ribosomal subunit

To elucidate the molecular details of MERS-CoV Nsp1 interaction with the 40S ribosomal subunit and understand the mechanistic basis for its translational inhibition, we carried out cryo-EM studies with recombinant MERS-CoV Nsp1 and human 40S ribosomal subunit purified from HEK293 cell lysates. We resolved a 2.6-Å reconstruction of the human 40S ribosomal subunit in complex with MERS-CoV Nsp1 (Figures 2A, S2, and S3). The high-resolution cryo-EM map allowed for unambiguous model building and identification of electron density attributable to MERS-CoV Nsp1 (Figures 2B and S4A and Tables S1 and S2). The CTD of MERS-CoV Nsp1 (167–193) folds into a "helix-turn-helix" motif that binds in the mRNA entry channel of the 40S subunit and forms an extensive network of interactions with the 18S ribosomal RNA (rRNA) and the ribosomal proteins uS3 and uS5 (Figure 2C). This binding mechanism is largely identical to SARS-CoV-2 Nsp1 despite modest sequence conservation between the two proteins (Figure S1A).[25,26]

The mRNA entry channel of the 40S ribosomal subunit is formed by the ribosomal proteins uS3, uS5, and helix 18 (h18) of the 18S rRNA. Helix 1 (residues 168–178) of MERS-CoV Nsp1 C-terminal motif is amphipathic, with several acidic

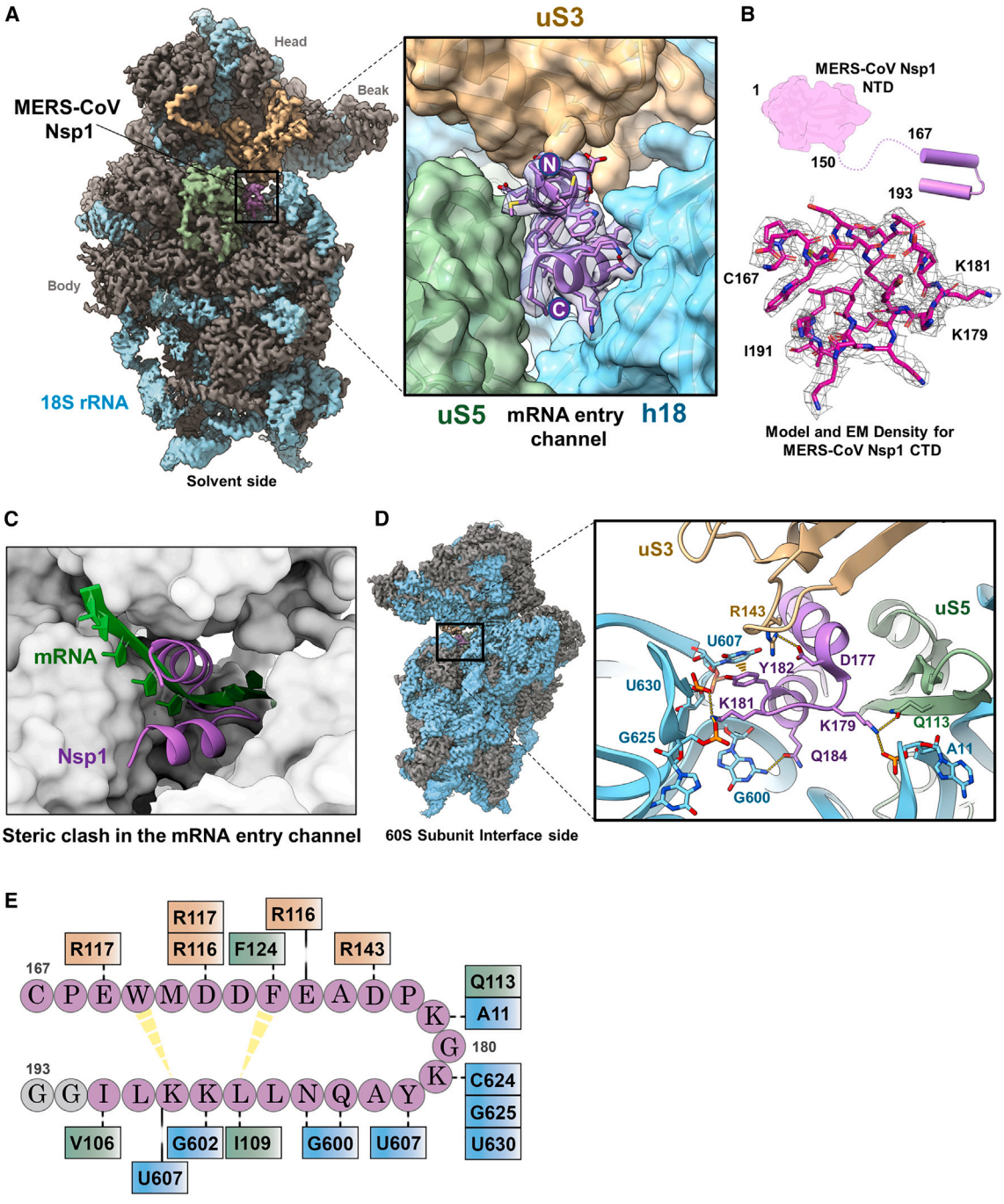

Figure 2. Cryo-EM structure of MERS-CoV Nsp1 bound to human 40S ribosomal subunit

(A) Overview of the cryo-EM structure of MERS-CoV Nsp1 bound to human 40S ribosomal subunit. The C-terminal domain of MERS-CoV Nsp1 forms a helix-turn-helix motif with extensive interactions in the mRNA entry channel (right inset).

(B) Schematic of MERS-CoV Nsp1 illustrating the unmodeled N-terminal domain as a purple blob and the modeled CTD connected by a linker. The amino acid numbers denoting the domain boundaries are also shown. Modeled region of MERS-CoV Nsp1 CTD is shown as an inset along with the corresponding cryo-EM density (bottom).

(C) Structure of MERS-CoV Nsp1-40S ribosome complex was aligned with the human 48S preinitiation complex (PDB: 6ZMW). The steric clash between the mRNA and MERS-CoV Nsp1 CTD in the mRNA entry channel is highlighted.

(legend continued on next page)

residues (E169, D172, D173, E175, and D177) that form ionic interactions with the positively charged surface of uS3 in the mRNA entry channel (Figures 2D, 2E, and S4B). The hydrophobic residues of helix 1 (W170, M171, and F174) pack against the hydrophobic residues of helix 2 (L186, L187, L190, I191) to form the hydrophobic core of MERS-CoV Nsp1 CTD. Furthermore, residues V106, I109, and F124 of uS5 stack against the hydrophobic core of the MERS-CoV Nsp1 CTD. The two helices of the MERS-CoV Nsp1 CTD are connected by a tight turn composed of K179, G180, and K181, wherein the two lysine residues extend deep into the mRNA entry channel and anchor the Nsp1 CTD. K179 of Nsp1 interacts with the phosphate oxygen of the nucleotide A11 of the 18S rRNA as well as with the amino acid Q113 of uS5. K181, on the other hand, forms close contacts with the phosphate backbone of C624, G625, and U630 of the 18S rRNA. Notably, the neighboring residue, Y182, at the start of helix 2 of the MERS-CoV Nsp1 CTD, forms a pi-stacking interaction with the nucleobase of U607. Interestingly, K181 and Y182 of the MERS-CoV Nsp1 form similar contacts with the 40S ribosomal subunit as the critical K164 and H165 residues of the SARS-CoV-2 Nsp1. Other MERS-CoV Nsp1 residues that interact with the 18S rRNA include Q184, N185, K188, and K189 (Figure 2E). The NTD of MERS-CoV Nsp1 is flexible in our structure, and the corresponding electron density is too weak for unambiguous model building. However, at lower contour level thresholds, a globular density is present between helix 16 (h16) of the 18S rRNA and the ribosomal protein uS3, which we attribute to the MERS-CoV NTD (Figure S4C). Similar to the MERS-CoV Nsp1, in all reported structures of SARS-CoV-2 Nsp1 with the 40S ribosome, the NTD was too weak for model building and placed between h16 of 18S rRNA and uS3.[5,13,19]

MERS-CoV Nsp1 CTD is critical for translation inhibition

To evaluate the functional importance of the key interactions observed in our structure, we made a series of structure-guided mutants of MERS-CoV Nsp1. The two lysines, K179 and K181, anchoring the CTD in the mRNA entry channel were mutated to generate the double mutant MERS KK (K179A/K181A). Similarly, to analyze the MERS KY motif, which mirrors the critical SARS-CoV-2 KH motif, residues K181 and Y182 were mutated to alanines for the double mutant MERS KY.[19] Lastly, we created a mutant, MERS ΔCT, which lacked the entire CTD (Δ165–193), leaving only the NTD and the linker region (1–164) (Figure 3A). The mutants were purified and tested for their ability to inhibit translation alongside WT MERS-CoV and SARS-CoV-2 Nsp1 (Figure S4D). Both WT MERS-CoV and SARS-CoV-2 Nsp1 showed high levels of translation inhibition (>90%) compared to the "No Nsp1" control (Figure 3B). The well-characterized SARS-CoV-2 mutant, K164A/H165A, showed minimal translation inhibition compared to WT SARS-CoV-2 Nsp1, in agreement with previously reported studies.[27,28] As predicted from the structural analysis, all three of the MERS-CoV Nsp1 mutants—MERS KK, MERS KY, and MERS ΔCT—abolished the translation inhibition compared to WT MERS-CoV Nsp1 (Figure 3B). These results suggest that the interaction between the CTD of MERS-CoV Nsp1 and the 40S ribosomal subunit is critical for its translation inhibition activity.

DISCUSSION

Nsp1 of β-CoVs is a critical pathogenicity factor, and among the β-CoVs that have caused significant outbreaks in the last three decades, MERS-CoV has the highest fatality rate.[2] Nsp1 of MERS-CoV also shows significant sequence divergence compared to SARS-CoV and SARS-CoV-2 Nsp1. Contrary to previous reports, herein we show that MERS-CoV Nsp1 directly interacts with the 40S ribosomal subunit and robustly inhibits protein translation. Despite modest sequence conservation, MERS-CoV Nsp1 exhibits a remarkably similar mechanism to SARS-CoV-2 Nsp1 by targeting the 40S ribosomal subunit and restricting host translation.

Interestingly, SARS-CoV-2 Nsp1 inhibits translation more potently than MERS-CoV Nsp1 (Figure 1A), even though the binding affinities of the two proteins to the 40S ribosomal subunit are in a similar range, with SARS-CoV-2 Nsp1 having the higher affinity (Figure 1B). Therefore, we speculate this observed difference in potency is due to effects beyond initial binding to the 40S ribosomal subunit. Nsp1 has been reported to drive mRNA cleavage in a ribosome-dependent manner[17,23] and to interact with several other cellular factors.[29] These additional functionalities and interactions remain poorly characterized, and we suspect they may be responsible for the differential potency between SARS-CoV-2 and MERS-CoV Nsp1. Future studies investigating these additional roles of the NTD, the linker region, and potential interacting cellular factors are needed to gain a deeper understanding of the differences in the translation inhibition potency of Nsp1 from various β-CoVs.

Eukaryotic translation initiation is a highly regulated process involving an ensemble of translation initiation factors that interact with the 40S ribosomal subunit to form the 43S[30–32] and 48S preinitiation complexes.[33–35] mRNA loading on the 40S ribosome during translation initiation is a highly regulated event, and the details of this process have remained elusive. However, recent structure-based models highlight the importance of the "mRNA latch" formed by the ribosomal protein uS3 and h18 and h34 of the 18S rRNA.[33,36–38] The "open" state of the mRNA latch is required for mRNA loading, whereas the "closed" state regulates 5′ UTR scanning. Upon analyzing and comparing our structure to previous structures of the 43S and 48S preinitiation complexes, it was apparent that the mRNA latch was in a "closed" state, and the extensive interactions of MERS-CoV Nsp1 CTD with uS3, uS5, and h34 of the 18S rRNA appear to stabilize the "closed" state (Figure 3C). Interestingly, the previously reported SARS-CoV-2 Nsp1 structures bound to 40S ribosome

(D) MERS-CoV Nsp1 interaction within the mRNA entry channel is shown from the 60S subunit interface side of the 40S ribosome. Key interactions between 18S rRNA, uS3 and uS5, and MERS-CoV Nsp1 are highlighted.

(E) The overall interaction map of MERS-CoV Nsp1 CTD with 40S ribosome is represented schematically. The MERS-CoV Nsp1 residues (purple) and the interacting residues from 40S ribosome–uS3 (brown), us5 (green), and 18S rRNA (cyan)–are shown. The key hydrophobic packing interactions within MERS-CoV Nsp1 CTD are highlighted in yellow. Also refer to Figures S2, S3, and S4 and Tables S1 and S2.

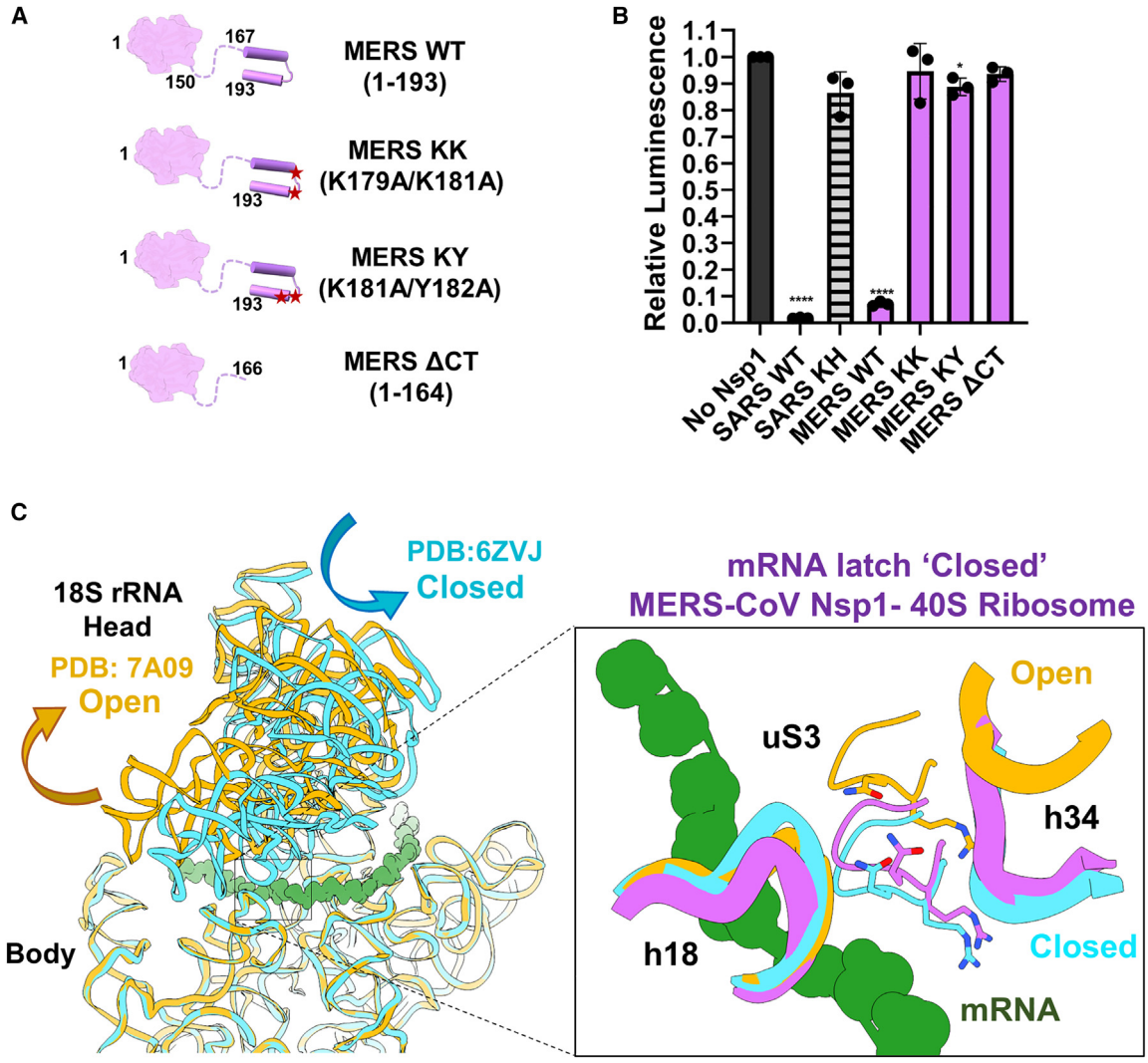

Figure 3. MERS-CoV Nsp1 CTD is critical for translation inhibition

(A) Schematic representation of the structure-guided mutants.

(B) *In vitro* protein translation of luciferase mRNA in the presence of WT and structure-guided mutants of MERS-CoV Nsp1 (6 μM). Data are the mean of three biological replicates +/− one standard deviation. Each biological replicate is the average of three technical replicates. Values for Nsp1-containing reactions were compared to the "No Nsp1" control using two-tailed, unpaired Student's t tests. *$p < 0.05$, ****$p < 0.0001$.

(C) Model for the mechanism of action for MERS-CoV Nsp1 inhibition of protein translation. The 18S rRNA from the "open" (orange) and "closed" (cyan) conformations of 40S ribosome is shown to highlight the motion of the 40S head (left). 48S PIC structure (PDB: 6ZMW) was also aligned, and only mRNA (green) is shown to highlight the mRNA path. MERS-CoV Nsp1 binding in the mRNA entry channel occludes the mRNA path, and overlaying the structures of 43S initiation complexes in the "open" (orange, PDB:7A09) and "closed" (cyan, PDB:6ZVJ) with our structure (purple, MERS-CoV Nsp1 not shown) revealed that MERS-CoV Nsp1 locks the mRNA "latch" in the closed position (right inset). Also refer to Figure S4.

also adopt this same conformation.[5,13,19] Thus, Nsp1 from all β-CoVs may share a common mechanism of trapping the 40S ribosomal subunit in a conformation wherein the mRNA latch is in the "closed" position, preventing conformational changes necessary for mRNA loading and abrogating translation initiation (Figure 3C).

The COVID-19 pandemic has proved to be extremely deadly, causing nearly 15 million deaths by early 2023,[39] yet still a vast zoonotic reservoir of novel β-CoVs looms as a threat for future pandemics.[40] Even within the COVID-19 pandemic, evolutionary pressures have caused rapid antigenic drift in SARS-CoV-2 spike protein, rendering current vaccines as a limited solution.[41,42] Therefore, diversified therapeutics targeting multiple stages of the viral life cycle will be critical for containing current and future outbreaks. As Nsp1 of β-CoVs is an essential pathogenicity factor, it presents an attractive target for therapeutic intervention.[43] Our results here provide a structural basis for MERS-CoV Nsp1 translation inhibition, and despite large sequence divergence from SARS-CoV-2 Nsp1, both proteins share a conserved mechanism to bind the mRNA entry channel

of the 40S ribosomal subunit. Combined with previous structural studies on SARS-CoV-2 Nsp1, our results presented here provide a roadmap to the critical features of β-CoV Nsp1-40S ribosome interaction and will aid in the development of therapeutics that can target Nsp1 proteins across β-CoVs.

Limitations of the study

Our study provides molecular level details for MERS-CoV Nsp1 interaction with the mRNA entry channel of the 40S ribosome. However, we could not resolve the NTD of MERS-CoV Nsp1 at a high resolution, and thus the mechanistic role of the MERS-CoV Nsp1 NTD in translation inhibition remains uncharacterized. Since we used purified components for our structural studies, it is possible that stable binding of MERS-CoV Nsp1 NTD to the 40S ribosome requires additional cellular components that are missing from our current experimental setup. In addition, our study did not investigate the roles of various mRNA 5′ UTRs on the translation inhibition effects of MERS-CoV and SARS-CoV-2 Nsp1. The importance of the viral 5′ UTR in escaping the translation inhibition by its own Nsp1 has been shown previously,[17,44,45] and extensive future studies are needed to understand the molecular basis behind this phenomenon.

STAR★METHODS

Detailed methods are provided in the online version of this paper and include the following:

- KEY RESOURCES TABLE
- RESOURCE AVAILABILITY
  - Lead contact
  - Materials availability
  - Data and code availability
- EXPERIMENTAL MODEL AND STUDY PARTICIPANT DETAILS
- METHOD DETAILS
  - Bacterial Expression and Purification of Recombinant Nsp1 Proteins
  - Purification of 40S ribosomal subunits
  - Co-pelleting of Nsp1:40S Ribosomal Subunit Complexes by Ultracentrifugation
  - *In vitro* Transcription of Luciferase mRNA
  - *In vitro* translation of luciferase mRNA
  - Plasmids and cloning
  - Cryo-EM Sample Preparation and Data Collection
  - Cryo-EM data processing and model Building
  - Fluorescein-5-maleimide conjugation to Nsp1
  - Fluorescence polarization-based titrations
- QUANTIFICATION AND STATISTICAL ANALYSIS

SUPPLEMENTAL INFORMATION

Supplemental information can be found online at https://doi.org/10.1016/j.celrep.2023.113156.

ACKNOWLEDGMENTS

We would like to acknowledge access to the EM resources at the Laboratory for BioMolecular Structure (LBMS) at Brookhaven National Lab and the Yale cryo-EM Core. We thank C. Lewis for providing the luciferase mRNA plasmid as well as *in vitro* translation reagents. We also thank F. Bleichert and D. Engelman for equipment access. The Laboratory for BioMolecular Structure (LBMS) is supported by the DOE Office of Biological and Environmental Research (KP1607011). This work was supported by DoD PRMRP IIAR (W81XWH-21-1-0019) to S.C., by NIH R01GM132358 to W.V.G., and by Yale discretionary funds to Y.X.

AUTHOR CONTRIBUTIONS

S.C.D. and M.V. contributed equally to this work. M.V., S.B., and I.B.L. purified the rabbit and human 40S ribosomes. M.V. and S.B. conducted the recombinant protein purifications. S.C.D conducted the cryo-EM data collection, data processing, and model building. D.J., W.G., and M.V. contributed to experimental design of *in vitro* translation assays. M.V. conducted the *in vitro* translation assays. Y.L. and C.S. contributed to data analysis. S.B. conducted the co-pelleting ultracentrifugation assays. S.C.D. and M.V. conducted the fluorescein labeling of proteins. S.C.D performed the fluorescence polarization experiments. S.C.D., M.V., and Y.X. prepared the manuscript; all authors contributed to editing. Y.X. supervised the project.

DECLARATION OF INTERESTS

Y.X. serves on the advisory board of *Cell Reports*.

INCLUSION AND DIVERSITY

We support inclusive, diverse, and equitable conduct of research.

Received: June 16, 2023
Revised: August 13, 2023
Accepted: September 5, 2023
Published: September 19, 2023

REFERENCES

1. Chan-Yeung, M., and Xu, R.H. (2003). SARS: epidemiology. Respirology *8 Suppl* (*Suppl*), S9–S14. https://doi.org/10.1046/j.1440-1843.2003.00518.x.
2. Zhang, A.R., Shi, W.Q., Liu, K., Li, X.L., Liu, M.J., Zhang, W.H., Zhao, G.P., Chen, J.J., Zhang, X.A., Miao, D., et al. (2021). Epidemiology and evolution of Middle East respiratory syndrome coronavirus, 2012-2020. Infect. Dis. Poverty *10*, 66. https://doi.org/10.1186/s40249-021-00853-0.
3. Hasan, M.N., Haider, N., Stigler, F.L., Khan, R.A., McCoy, D., Zumla, A., Kock, R.A., and Uddin, M.J. (2021). The Global Case-Fatality Rate of COVID-19 Has Been Declining Since May 2020. Am. J. Trop. Med. Hyg. *104*, 2176–2184. https://doi.org/10.4269/ajtmh.20-1496.
4. Kumar, A., Ishida, R., Strilets, T., Cole, J., Lopez-Orozco, J., Fayad, N., Felix-Lopez, A., Elaish, M., Evseev, D., Magor, K.E., et al. (2021). SARS-CoV-2 Nonstructural Protein 1 Inhibits the Interferon Response by Causing Depletion of Key Host Signaling Factors. J. Virol. *95*, e0026621. https://doi.org/10.1128/JVI.00266-21.
5. Yuan, S., Peng, L., Park, J.J., Hu, Y., Devarkar, S.C., Dong, M.B., Shen, Q., Wu, S., Chen, S., Lomakin, I.B., and Xiong, Y. (2020). Nonstructural Protein 1 of SARS-CoV-2 Is a Potent Pathogenicity Factor Redirecting Host Protein Synthesis Machinery toward Viral RNA. Mol. Cell *80*, 1055–1066.e6. https://doi.org/10.1016/j.molcel.2020.10.034.
6. Fisher, T., Gluck, A., Narayanan, K., Kuroda, M., Nachshon, A., Hsu, J.C., Halfmann, P.J., Yahalom-Ronen, Y., Tamir, H., Finkel, Y., et al. (2022). Parsing the role of NSP1 in SARS-CoV-2 infection. Cell Rep. *39*, 110954. https://doi.org/10.1016/j.celrep.2022.110954.
7. Nakagawa, K., and Makino, S. (2021). Mechanisms of Coronavirus Nsp1-Mediated Control of Host and Viral Gene Expression. Cells *10*. https://doi.org/10.3390/cells10020300.

8. Min, Y.Q., Mo, Q., Wang, J., Deng, F., Wang, H., and Ning, Y.J. (2020). SARS-CoV-2 nsp1: Bioinformatics, Potential Structural and Functional Features, and Implications for Drug/Vaccine Designs. Front. Microbiol. *11*, 587317. https://doi.org/10.3389/fmicb.2020.587317.

9. Almeida, M.S., Johnson, M.A., Herrmann, T., Geralt, M., and Wüthrich, K. (2007). Novel beta-barrel fold in the nuclear magnetic resonance structure of the replicase nonstructural protein 1 from the severe acute respiratory syndrome coronavirus. J. Virol. *81*, 3151–3161. https://doi.org/10.1128/JVI.01939-06.

10. Chaudhuri, A. (2021). Comparative analysis of non structural protein 1 of SARS-CoV2 with SARS-CoV1 and MERS-CoV: An in silico study. J. Mol. Struct. *1243*, 130854. https://doi.org/10.1016/j.molstruc.2021.130854.

11. Wang, Y., Kirkpatrick, J., Lage, S.Z., and Carlomagno, T. (2023). Structural insights into the activity regulation of full-length non-structural protein 1 from SARS-CoV-2. Structure *31*, 128–137.e5. https://doi.org/10.1016/j.str.2022.12.006.

12. Clark, L.K., Green, T.J., and Petit, C.M. (2021). Structure of Nonstructural Protein 1 from SARS-CoV-2. J. Virol. *95*, e02019-20. https://doi.org/10.1128/JVI.02019-20.

13. Thoms, M., Buschauer, R., Ameismeier, M., Koepke, L., Denk, T., Hirschenberger, M., Kratzat, H., Hayn, M., Mackens-Kiani, T., Cheng, J., et al. (2020). Structural basis for translational shutdown and immune evasion by the Nsp1 protein of SARS-CoV-2. Science *369*, 1249–1255. https://doi.org/10.1126/science.abc8665.

14. Jumper, J., Evans, R., Pritzel, A., Green, T., Figurnov, M., Ronneberger, O., Tunyasuvunakool, K., Bates, R., Žídek, A., Potapenko, A., et al. (2021). Highly accurate protein structure prediction with AlphaFold. Nature *596*, 583–589. https://doi.org/10.1038/s41586-021-03819-2.

15. Bhatt, P.R., Scaiola, A., Loughran, G., Leibundgut, M., Kratzel, A., Meurs, R., Dreos, R., O'Connor, K.M., McMillan, A., Bode, J.W., et al. (2021). Structural basis of ribosomal frameshifting during translation of the SARS-CoV-2 RNA genome. Science *372*, 1306–1313. https://doi.org/10.1126/science.abf3546.

16. Mendez, A.S., Ly, M., González-Sánchez, A.M., Hartenian, E., Ingolia, N.T., Cate, J.H., and Glaunsinger, B.A. (2021). The N-terminal domain of SARS-CoV-2 nsp1 plays key roles in suppression of cellular gene expression and preservation of viral gene expression. Cell Rep. *37*, 109841. https://doi.org/10.1016/j.celrep.2021.109841.

17. Kamitani, W., Huang, C., Narayanan, K., Lokugamage, K.G., and Makino, S. (2009). A two-pronged strategy to suppress host protein synthesis by SARS coronavirus Nsp1 protein. Nat. Struct. Mol. Biol. *16*, 1134–1140. https://doi.org/10.1038/nsmb.1680.

18. Zhang, K., Miorin, L., Makio, T., Dehghan, I., Gao, S., Xie, Y., Zhong, H., Esparza, M., Kehrer, T., Kumar, A., et al. (2021). Nsp1 protein of SARS-CoV-2 disrupts the mRNA export machinery to inhibit host gene expression. Sci. Adv. *7*, eabe7386. https://doi.org/10.1126/sciadv.abe7386.

19. Schubert, K., Karousis, E.D., Jomaa, A., Scaiola, A., Echeverria, B., Gurzeler, L.A., Leibundgut, M., Thiel, V., Mühlemann, O., and Ban, N. (2020). Author Correction: SARS-CoV-2 Nsp1 binds the ribosomal mRNA channel to inhibit translation. Nat. Struct. Mol. Biol. *27*, 1094. https://doi.org/10.1038/s41594-020-00533-x.

20. Lokugamage, K.G., Narayanan, K., Nakagawa, K., Terasaki, K., Ramirez, S.I., Tseng, C.T.K., and Makino, S. (2015). Middle East Respiratory Syndrome Coronavirus nsp1 Inhibits Host Gene Expression by Selectively Targeting mRNAs Transcribed in the Nucleus while Sparing mRNAs of Cytoplasmic Origin. J. Virol. *89*, 10970–10981. https://doi.org/10.1128/JVI.01352-15.

21. Pan, Z., Feng, Y., Wang, Z., Lei, Z., Han, Q., and Zhang, J. (2022). MERS-CoV nsp1 impairs the cellular metabolic processes by selectively downregulating mRNAs in a novel granules. Virulence *13*, 355–369. https://doi.org/10.1080/21505594.2022.2032928.

22. Tidu, A., Janvier, A., Schaeffer, L., Sosnowski, P., Kuhn, L., Hammann, P., Westhof, E., Eriani, G., and Martin, F. (2020). The viral protein NSP1 acts as a ribosome gatekeeper for shutting down host translation and fostering SARS-CoV-2 translation. RNA, 120. https://doi.org/10.1261/rna.078121.

23. Bujanic, L., Shevchuk, O., von Kügelgen, N., Kalinina, A., Ludwik, K., Koppstein, D., Zerna, N., Sickmann, A., and Chekulaeva, M. (2022). The key features of SARS-CoV-2 leader and NSP1 required for viral escape of NSP1-mediated repression. RNA *28*, 766–779. https://doi.org/10.1261/rna.079086.121.

24. Narayanan, K., Ramirez, S.I., Lokugamage, K.G., and Makino, S. (2015). Coronavirus nonstructural protein 1: Common and distinct functions in the regulation of host and viral gene expression. Virus Res. *202*, 89–100. https://doi.org/10.1016/j.virusres.2014.11.019.

25. Edgar, R.C. (2004). MUSCLE: multiple sequence alignment with high accuracy and high throughput. Nucleic Acids Res. *32*, 1792–1797. https://doi.org/10.1093/nar/gkh340.

26. Thompson, J.D., Higgins, D.G., and Gibson, T.J. (1994). CLUSTAL W: improving the sensitivity of progressive multiple sequence alignment through sequence weighting, position-specific gap penalties and weight matrix choice. Nucleic Acids Res. *22*, 4673–4680. https://doi.org/10.1093/nar/22.22.4673.

27. Frolov, I., Agback, T., Palchevska, O., Dominguez, F., Lomzov, A., Agback, P., and Frolova, E.I. (2023). All Domains of SARS-CoV-2 nsp1 Determine Translational Shutoff and Cytotoxicity of the Protein. J. Virol. *97*, e0186522. https://doi.org/10.1128/jvi.01865-22.

28. Lapointe, C.P., Grosely, R., Johnson, A.G., Wang, J., Fernández, I.S., and Puglisi, J.D. (2021). Dynamic competition between SARS-CoV-2 NSP1 and mRNA on the human ribosome inhibits translation initiation. Proc. Natl. Acad. Sci. USA *118*, e2017715118. https://doi.org/10.1073/pnas.2017715118.

29. Gordon, D.E., Hiatt, J., Bouhaddou, M., Rezelj, V.V., Ulferts, S., Braberg, H., Jureka, A.S., Obernier, K., Guo, J.Z., Batra, J., et al. (2020). Comparative host-coronavirus protein interaction networks reveal pan-viral disease mechanisms. Science *370*, eabe9403. https://doi.org/10.1126/science.abe9403.

30. Kratzat, H., Mackens-Kiani, T., Ameismeier, M., Potocnjak, M., Cheng, J., Dacheux, E., Namane, A., Berninghausen, O., Herzog, F., Fromont-Racine, M., et al. (2021). A structural inventory of native ribosomal ABCE1-43S pre-initiation complexes. EMBO J. *40*, e105179. https://doi.org/10.15252/embj.2020105179.

31. Hashem, Y., des Georges, A., Dhote, V., Langlois, R., Liao, H.Y., Grassucci, R.A., Hellen, C.U.T., Pestova, T.V., and Frank, J. (2013). Structure of the mammalian ribosomal 43S preinitiation complex bound to the scanning factor DHX29. Cell *153*, 1108–1119. https://doi.org/10.1016/j.cell.2013.04.036.

32. Hinnebusch, A.G. (2014). The scanning mechanism of eukaryotic translation initiation. Annu. Rev. Biochem. *83*, 779–812. https://doi.org/10.1146/annurev-biochem-060713-035802.

33. Brito Querido, J., Sokabe, M., Kraatz, S., Gordiyenko, Y., Skehel, J.M., Fraser, C.S., and Ramakrishnan, V. (2020). Structure of a human 48S translational initiation complex. Science *369*, 1220–1227. https://doi.org/10.1126/science.aba4904.

34. Eliseev, B., Yeramala, L., Leitner, A., Karuppasamy, M., Raimondeau, E., Huard, K., Alkalaeva, E., Aebersold, R., and Schaffitzel, C. (2018). Structure of a human cap-dependent 48S translation pre-initiation complex. Nucleic Acids Res. *46*, 2678–2689. https://doi.org/10.1093/nar/gky054.

35. Sonenberg, N., and Hinnebusch, A.G. (2009). Regulation of translation initiation in eukaryotes: mechanisms and biological targets. Cell *136*, 731–745. https://doi.org/10.1016/j.cell.2009.01.042.

36. Jobe, A., Liu, Z., Gutierrez-Vargas, C., and Frank, J. (2019). New Insights into Ribosome Structure and Function. Cold Spring Harbor Perspect. Biol. *11*, a032615. https://doi.org/10.1101/cshperspect.a032615.

37. Lomakin, I.B., and Steitz, T.A. (2013). The initiation of mammalian protein synthesis and mRNA scanning mechanism. Nature *500*, 307–311. https://doi.org/10.1038/nature12355.

38. Llácer, J.L., Hussain, T., Marler, L., Aitken, C.E., Thakur, A., Lorsch, J.R., Hinnebusch, A.G., and Ramakrishnan, V. (2015). Conformational Differences between Open and Closed States of the Eukaryotic Translation Initiation Complex. Mol. Cell *59*, 399–412. https://doi.org/10.1016/j.molcel.2015.06.033.

39. Msemburi, W., Karlinsky, A., Knutson, V., Aleshin-Guendel, S., Chatterji, S., and Wakefield, J. (2023). The WHO estimates of excess mortality associated with the COVID-19 pandemic. Nature *613*, 130–137. https://doi.org/10.1038/s41586-022-05522-2.

40. Ruiz-Aravena, M., McKee, C., Gamble, A., Lunn, T., Morris, A., Snedden, C.E., Yinda, C.K., Port, J.R., Buchholz, D.W., Yeo, Y.Y., et al. (2022). Author Correction: Ecology, evolution and spillover of coronaviruses from bats. Nat. Rev. Microbiol. *20*, 315. https://doi.org/10.1038/s41579-022-00691-3.

41. Yuan, M., Huang, D., Lee, C.C.D., Wu, N.C., Jackson, A.M., Zhu, X., Liu, H., Peng, L., van Gils, M.J., Sanders, R.W., et al. (2021). Structural and functional ramifications of antigenic drift in recent SARS-CoV-2 variants. Science *373*, 818–823. https://doi.org/10.1126/science.abh1139.

42. Kurup, D., Myers, J., and Schnell, M.J. (2022). Current vaccine strategies against SARS-CoV-2: Promises and challenges. J. Allergy Clin. Immunol. *150*, 17–21. https://doi.org/10.1016/j.jaci.2022.05.008.

43. Afsar, M., Narayan, R., Akhtar, M.N., Das, D., Rahil, H., Nagaraj, S.K., Eswarappa, S.M., Tripathi, S., and Hussain, T. (2022). Drug targeting Nsp1-ribosomal complex shows antiviral activity against SARS-CoV-2. Elife *11*. https://doi.org/10.7554/eLife.74877.

44. Terada, Y., Kawachi, K., Matsuura, Y., and Kamitani, W. (2017). MERS coronavirus nsp1 participates in an efficient propagation through a specific interaction with viral RNA. Virology *511*, 95–105. https://doi.org/10.1016/j.virol.2017.08.026.

45. Sosnowski, P., Tidu, A., Eriani, G., Westhof, E., and Martin, F. (2022). Correlated sequence signatures are present within the genomic 5'UTR RNA and NSP1 protein in coronaviruses. RNA *28*, 729–741. https://doi.org/10.1261/rna.078972.121.

46. Lomakin, I.B., Stolboushkina, E.A., Vaidya, A.T., Zhao, C., Garber, M.B., Dmitriev, S.E., and Steitz, T.A. (2017). Crystal Structure of the Human Ribosome in Complex with DENR-MCT-1. Cell Rep. *20*, 521–528. https://doi.org/10.1016/j.celrep.2017.06.025.

47. Rojas-Duran, M.F., and Gilbert, W.V. (2012). Alternative transcription start site selection leads to large differences in translation activity in yeast. RNA *18*, 2299–2305. https://doi.org/10.1261/rna.035865.112.

48. Punjani, A., Rubinstein, J.L., Fleet, D.J., and Brubaker, M.A. (2017). cryoSPARC: algorithms for rapid unsupervised cryo-EM structure determination. Nat. Methods *14*, 290–296. https://doi.org/10.1038/nmeth.4169.

49. Emsley, P., Lohkamp, B., Scott, W.G., and Cowtan, K. (2010). Features and development of Coot. Acta Crystallogr. D Biol. Crystallogr. *66*, 486–501. https://doi.org/10.1107/S0907444910007493.

50. Liebschner, D., Afonine, P.V., Baker, M.L., Bunkóczi, G., Chen, V.B., Croll, T.I., Hintze, B., Hung, L.W., Jain, S., McCoy, A.J., et al. (2019). Macromolecular structure determination using X-rays, neutrons and electrons: recent developments in Phenix. Acta Crystallogr. D Struct. Biol. *75*, 861–877. https://doi.org/10.1107/S2059798319011471.

51. Schneider, C.A., Rasband, W.S., and Eliceiri, K.W. (2012). NIH Image to ImageJ: 25 years of image analysis. Nat. Methods *9*, 671–675. https://doi.org/10.1038/nmeth.2089.

STAR★METHODS

KEY RESOURCES TABLE

REAGENT or RESOURCE	SOURCE	IDENTIFIER
Antibodies		
His-Tag Monoclonal antibody	ProteinTech	Cat# CL594-66005; RRID: AB_2883473
Goat Anti-Mouse IgG HRP	Cayman Chemical Company	Cat# 10004302; RRID: AB_10078261
Bacterial and virus strains		
DH5α	New England Biosciences	C2987H
BL21 (DE3)	New England Biosciences	C2527H
Chemicals, peptides, and recombinant proteins		
Ulp1 Protease (*Saccharomyces cerevisiae*)	Xiong Lab Purified Protein Stocks	Accession number 1EUV_A (amino acids 1–221)
Creatine Kinase	Millipore Sigma/Roche	10127566001
Creatine Phosphate	Thermo Fisher	337340100
Complete, Mini Protease Inhibitor Cocktail	Roche	11836153001
Potassium Chloride	Sigma-Aldrich	P9541
Magnesium Acetate	Sigma-Aldrich	M5661
EDTA	Sigma-Aldrich	E5134
DTT	GoldBio	27565-41-9
Ammonium Acetate	Sigma-Aldrich	A1542
SUPERase-in	Invitrogen	AM2696
Sac1HF	NEB	R3156S
HEPES KOH	Sigma-Aldrich	H0527
Spermidine HCl	Sigma-Aldrich	S2626
ATP	Jena Bioscience	NU-1010
GTP	ThermoScientific	R0461
CHAPSO	EMD Millipore	220202
Potassium glutamate	Sigma-Aldrich	236497
Magnesium glutamate	Sigma-Aldrich	M0631
Creatine phosphate	Thermo Fisher	A15362.06
HeLa cytoplasmic extract	Ipracell	CC-01-40-50
Fluorescein-5-Maleimide	ThermoFisher Scientific	62245
Potassium Acetate	JT Baker	2912–01
Magnesium Chloride	Sigma-Aldrich	63068
Dithiothreitol (DTT)	Fisher Scientific	BP17225
Clarity Western ECL substrate	Bio-Rad	1705060S
10x TBS Buffer	Bio-Rad	1706435
Tween 20	Sigma-Aldrich	P7949
Instant Nonfat Dry Milk	Nestle/Carnation	12428935
isopropyl β-D-1-thiogalactopyranoside	GoldBio	I2481C100
NaCl	AmericanBio	AB01915
Tris-HCl	AmericanBio	AB14044
TCEP	GoldBio	TCEP25
Luria Broth	Research Products International	31FZ61
Terrific Broth	Research Products International	31GE05
Rabbit Reticulocyte Lysate	Green Hectares	N/A
Kanamycin	ThermoScientific	450810100

(*Continued on next page*)

Continued

REAGENT or RESOURCE	SOURCE	IDENTIFIER
Ampicillin	GoldBio	A-301-100
Phenol:Chloroform:IAA	Invitrogen	15593–031
Chloroform	JT Baker	9180–01
Isoamyl alcohol	JT Baker	9038–01
Ethanol	Sigma-Aldrich	E7023
Critical commercial assays		
Luciferase Assay System	Promega	E1500
mMessage mMachine T7 transcription kit	Invitrogen	AM1344
Gibson assembly cloning	New England Biosciences	E5510S
Q5 High-Fidelity DNA Polymerase	New England Biosciences	M0491L
Deposited data		
MERS-CoV Nsp1 bound human 40S ribosomal subunit	PDB	8T4S
Electron density map (focus refined composite map)	EMDB	EMD-41039
Electron density map (consensus refined map)	EMDB	EMD-41063
Electron density map (focus refined 40S head map)	EMDB	EMD-41064
Electron density map (focus refined 40S body map)	EMDB	EMD-41065
Experimental models: Organisms/strains		
Middle East Respiratory Syndrome	NIH GenBank	WBY50300.1 (Amino acids 1–193)
Severe Acute Respiratory Syndrome Coronavirus 2	NIH GenBank	YP_009725297.1 (Amino acids 1–180)
Oligonucleotides		
SARS-CoV-2 Nsp1 KH Forward (CCAGGAAAACTGGAACACCGCGGCC CAGCTCCGGAGTGACCAGAGAGCTG)	IDT	N/A
SARS-CoV-2 Nsp1 KH Reverse (CACTCCGGAGCTGTGCTTGGGCCGC GGTGTTCCAGTTTTCCTGGAAGTCC)	IDT	N/A
MERS Nsp1 KY Forward (CTAAAGGCGCAGCTGCCC AGAATCTGCTTAAG)	IDT	N/A
MERS Nsp1 KY Reverse (CTGGGCAGCTGCGCCTTTAGGA TCCGCCTCAAAATC)	IDT	N/A
MERS Nsp1 KK Forward (GCGGATCCTGCAGGCGCATATG CCCAGAATCTGCTTAAGAAGTTG)	IDT	N/A
MERS Nsp1 KK Reverse (GCAGATTCTGGGCATATGCGCCTGCA GGATCCGCCTCAAAATCGTCCATCCAC)	IDT	N/A
MERS ΔCT Forward (CATTCCACTATGAGCGAGACAACT AACTCGAGCACCACCACCACC)	IDT	N/A
MERS ΔCT Reverse (GGTGGTGGTGGTGCTCGAGTTA GTTGTCTCGCTCATAGTGGAATG)	IDT	N/A

(*Continued on next page*)

Continued

REAGENT or RESOURCE	SOURCE	IDENTIFIER
Cys SARS2 Nsp1 Forward (GGAGGTTCAGGTGGAGGTGGAT CAGGTTCTTGCTAACTCGAGCAC CACCACCACCACTG)	IDT	N/A
Cys SARS2 Nsp1 Reverse (GCAAGAACCTGATCCACCTCCAC CTGAACCTCCGCCACCGTTCAGT TCACGCATCAGC)	IDT	N/A
Recombinant DNA		
SARS2 WT	This Paper	N/A
SARS2 KH	This Paper	N/A
MERS WT	This Paper	N/A
MERS KY	This Paper	N/A
MERS KK	This Paper	N/A
MERS ΔCT	This Paper	N/A
Luciferase Reporter mRNA plasmid	Gilbert Lab	N/A
Cys SARS2 Nsp1	This Paper	N/A
Cys MERS Nsp1	This Paper	N/A
Software and algorithms		
Adobe Illustrator	Adobe	2022
Adobe Photoshop	Adobe	2022
ImageJ	NIH	https://imagej.nih.gov/ij/download.html
CryoSparc	Structura Biotechnology Inc.	Version 4.2
Coot	N/A	Version 0.9.8.5
PHENIX	N/A	Version 1.2
Prism GraphPad	N/A	Version 9
Other		
C-flat R2/1 holey carbon copper grids	EMS	CF312-25
PVDF Membrane	Bio-Rad	1620177
Vitrobot Mark IV	ThermoFisher Scientific	N/A
Pelco easiGlow	Ted Pella	N/A

RESOURCE AVAILABILITY

Lead contact

Further information and requests for resources and reagents should be directed to and will be fulfilled by the lead contact, Yong Xiong (yong.xiong@yale.edu).

Materials availability

Plasmids generated in this study are available upon request from the lead contact, Yong Xiong.

Data and code availability

- The atomic model for MERS-CoV Nsp1 bound human 40S ribosomal subunit is deposited in the Protein DataBank (PDB) under the accession code PDB: 8T4S. The corresponding electron density maps are deposited in the Electron Microscopy DataBank (EMDB) under the accession code EMD: 41039 (focus refined composite map), EMD: 41063 (consensus refined map), EMD: 41064 (focus refined 40S head map) EMD: 41065 (focus refined 40S body map).
- This paper does not report original code.
- Any additional information required to reanalyze the data reported in this work paper is available from the lead contact upon request.

EXPERIMENTAL MODEL AND STUDY PARTICIPANT DETAILS

E. coli DH5α cells were used for all recombinant DNA cloning and plasmid amplification. E. coli BL21 cells were used for recombinant protein expression. All bacterial cultures were grown in the presence of the appropriate antibiotic, either ampicillin (100 μg/ml) or kanamycin (50 μg/ml). Bacterial colonies that were grown on LB agar plates were not used if over 1 week old. Bacterial cultures were grown at 37°C with orbital shaking at a speed of 180rpm under aerobic conditions in baffled flasks. The volume of the liquid cultures did not exceed one-third of the total flask volume, and the density of liquid cultures was monitored by OD_{600}. All recombinant protein inductions were initiated when cultures reached an OD_{600} of 0.6–0.8. Bacteria cultures were grown in either Luria Broth or Terrific Broth media.

METHOD DETAILS

Bacterial Expression and Purification of Recombinant Nsp1 Proteins

Full-length Nsp1 was cloned into pET28a protein expression vector with an N-terminal His_6-MBP-Sumo tag directly upstream of the Nsp1 coding region. *Escherichia coli* BL21 (DE3) cells were used for protein expression and were induced by 1.0 or 2.0 mM isopropyl β-D-1-thiogalactopyranoside (IPTG) at either 16°C for 20 h or 30°C for 3.5 h in Terrific Broth Media in the presence of appropriate antibiotic (see experimental models). Cells were harvested via centrifugation, resuspended in lysis buffer [50mM Tris-HCl, 500mM NaCl, 5% glycerol (v/v), 0.5mM TCEP, pH 7.4 at 4°C], and subsequently lysed using a microfluidizer. The lysate was clarified by centrifugation and then applied to a MBPTrap column (Cytiva). Proteins were eluted in lysis buffer supplemented with 10mM Maltose and subsequently were treated with His_6 tagged Ulp1 protease for 16 h at 4°C. Cleavage was evaluated by SDS-PAGE analysis, and the cleavage reaction was loaded onto a Ni-NTA column. Cleaved Nsp1 proteins were collected in the flowthrough and wash fractions (15-40mM Imidazole respectively). Concentration of the Nsp1 was performed in Amicon Ultra-15 Centrifugal Filter Concentrators with a 10kDa cutoff. Subsequent size exclusion chromatography (HiLoad Superdex 75, GE healthcare) was performed in a buffer of 50 mM Tris, 250 mM NaCl, 5% glycerol (v/v), 0.5mM TCEP, pH 8.0 at 4°C. Purity of the proteins were analyzed by SDS-PAGE after each step. The SARS-CoV-2 K164A/H165A mutant (SARS2 KH) was purified previously in a similar fashion. Full length His_6_MBP_SARS2 KH was expressed in Escherichia coli BL21 and treated identically as above through the stage of lysis by microfluidizer, but was purified by using Ni-NTA affinity, followed by anion exchange (Q Sepharose) and size exclusion chromatography.

Purification of 40S ribosomal subunits

40S ribosomal subunits were purified from either HEK293 cells or rabbit reticulocyte lysate (Green Hectares, USA) adhering to previously published protocols.[37,46] Rabbit reticulocyte lysate (RRL) was thawed and supplemented to contain the following [5mM HEPES-KOH (pH 7.1), 15mM KCl, 11mM MgOAc, 1.0mM EDTA (pH 8.0), 2mM DTT, 1x of Complete Protease Inhibitor Cocktail (Roche)]. Ribosomes were pelleted by ultracentrifugation at 40,000 rpm (125,000 G) for 10.5 h in a Beckman Type 45 Ti rotor at 4°C through a 30% sucrose cushion [30% sucrose (w/v), 20mM Bis-Tris (pH 5.9), 200mM NH_4OAc, 300mM KCl, 10mM MgOAc, 5mM DTT]. The pellet was resuspended in low potassium salt buffer (20mM HEPES-KOH (pH 7.1), 30mM KCl, 11mM MgOAc, 1mM EDTA (pH8.0), 2mM DTT, 1x Complete Protease Inhibitor (Roche), 200 U ml^{-1} SUPERaseIN (Ambion)]. Ammonium chloride was added to the suspension to a final concentration of 0.4M and then mixed for 30 min at 4°C. The suspension was then spun at 16,000 G in a benchtop microcentrifuge for 10 min at 4°C. Subsequently, the supernatant was subjected to size exclusion chromatography on an S200 prep grade column equilibrated with 20mM Tris-HCl, 500mM KCl, 10mM $MgCl_2$, 5% (v/v) glycerol, 2mM DTT at a pH of 7.4. Fractions were collected and analyzed by SDS–PAGE. Fractions containing 80S ribosomes were combined, supplemented to a final concentration of 2.5 mM $MgCl_2$, 1% glycerol and concentrated until a OD_{260nm} was between 200 and 350 U ml^{-1}. In order to disassociate the 80S ribosomes, our sample was subsequently supplemented with 1 mM puromycin and were incubated at 37°C for 20 min, then at 25°C for 20 min and afterward on ice for 10 min. Chilled ribosomes were clarified by centrifugation in a benchtop microcentrifuge for 10 min at 16,000 G at 4°C, and the supernatant was directly loaded on a 10–40% sucrose density gradient [10–40% (w/v) sucrose, 20mM Tris-HCl, 500mM KCl, 5mM MgOAc, 2mM DTT, pH 7.4], using a Beckman SW 32 Ti rotor at 25,000 rpm for 14.5 h. Fractions from the sucrose density gradient were analyzed by SDS-PAGE. Fractions containing 40S subunits were combined, concentrated to 391 U ml^{-1} (measured by $OD_{260\ nm}$) and dialyzed overnight into a buffer containing 10mM HEPES-KOH, 100mM KCl, 5mM MgOAc, 5% (v/v) glycerol, 2mM DTT, pH 7.1. Sample purity was also validated by investigating particle size, homogeneity, and 2D class averages using negative stain electron microscopy. After SDS PAGE and negative stain electron microscopy confirmed appropriate profiles for pure 40S ribosomal subunits, small aliquots were flash frozen in liquid nitrogen and stored at −80°C.

Co-pelleting of Nsp1:40S Ribosomal Subunit Complexes by Ultracentrifugation

Purified His_6-Nsp1 samples were first spun at 14,000 rpm for 5 min to pellet aggregates. A 20 μL reaction was assembled with 4 μM Nsp1 and 0.4 μM purified 40S ribosome in a buffer of 20 mM HEPES KOH, 100 mM KAc, 2.5 mM $MgCl_2$, 1 mM DTT pH 7.5 at 25°C. The sample was incubated at 37°C for 20 min, then at room temperature (25°C) for 20 min. Then, it was layered on 500 μL of a 30% sucrose cushion (30% sucrose (w/v), 10 mM Tris-HCl, 100 mM NaCl, 1 mM $MgCl_2$) and centrifugated in the TLA-110 rotor in a Beckman Optima TLX benchtop ultracentrifuge at 60,000 RPM for 2.5 h at 25°C. Supernatant was discarded and pellet fractions were

resuspended and run on 4–12% SDS PAGE gels (GenScript) and subsequently semi-dry transferred onto PVDF membrane (Bio-Rad Laboratories) in a Trans-Blot Semi-Dry Transfer Cell (BioRad Laboratories) at 15V for 35 min. Membranes were blocked in 3% milk w/v (Carnation) 1xTBST solution (Bio-Rad Laboratories) for 1 h at room temperature prior to antibody probing. The following primary antibodies were used in 1x TBST buffer: His-tag [mouse, 1:5,000, ProteinTech (Cat #66005)], HRP-conjugated IgG secondary anti-mouse antibody [goat anti-mouse, 1:4,000, Cayman Chemical Company (Cat #10004302)]. Primary was incubated for overnight at 4°C and the secondary for 1 h at room temperature the following day. Membranes were incubated with Clarity Western ECL substrate (Bio-Rad Laboratories) and imaged using a Chemidoc Imaging System (Bio-Rad Laboratories).

In vitro Transcription of Luciferase mRNA

Generation of capped/polyadenylated *in vitro* transcribed luciferase mRNA was performed using the mMessage mMachine T7 transcription kit (Invitrogen) according to the manufacturer's protocol using linearized plasmid as a template. Briefly, the backbone for the template was adopted from a previous publication[47] with a T7 promoter directly upstream of the 5′UTR from the human gene BEX5 (brain-expressed X linked 5). This 5′UTR has been identified to efficiently initiate translation *in vitro* (unpublished data from Cole Lewis and Wendy Gilbert). Directly downstream of the 5′UTR is a firefly luciferase coding region, short 3′UTR, and an encoded 55 nucleotide-long polyA tail. Directly downstream of the polyA tail is a single SacI restriction site, and Sac1HF (New England Biosciences) was used to linearize the plasmid to be used as a template for the transcription reaction. Linear DNA was purified by phenol/chloroform extraction (Invitrogen), followed by chloroform:IAA (24:1, v/v) extraction, then ethanol (Sigma-Aldrich) precipitation, and subsequent resuspension in nuclease-free water. After the transcription reaction, newly transcribed mRNA was purified by Lithium Chloride precipitation (supplied by the mMessage mMachine T7 Transcription kit), resuspended in RNAse-free water, and quantified by a NanoDrop One (ThermoFisher Scientific).

In vitro translation of luciferase mRNA

In vitro translation reactions were set up on ice by first pipetting 1 μL of a working stock of Nsp1 or protein buffer into PCR tubes. Master mix was assembled such that a 10 μL reaction would contain 4 μL of HeLa cytoplasmic extract (Ipracell), 2 units of RNAse inhibitor (SUPERase-in RNase Inhibitor, Invitrogen), 1.0 μg of creatine kinase (derived from rabbit muscle, Millipore Sigma/Roche), 16 mM HEPES KOH pH 7.5, 0.1 mM spermidine, 0.8 mM ATP, 0.1 mM GTP, 40 mM K glutamate, 2 mM Mg glutamate, and 20 mM creatine phosphate. Master mix was then added to the reaction. Finally, *in vitro* transcribed luciferase mRNA was added to reaction to a final concentration of 10 μM and a final reaction volume of 10 μL. Reactions were incubated at 37°C for 30 min in a thermocycler. Then 9 μL of the translation reaction was used to detect luminescence by Promega's Luciferase Assay System following the manufacturer's recommendation using a TriStar LB 941 Luminometer (Berthold Technologies). Parallel experiments were performed as technical triplicates. The average value of a technical triplicate was treated as a single biological experiment, and three separate biological experiments comprised a biological triplicate in statistical analysis.

Plasmids and cloning

pET28a was used for cloning in *E. coli* DH5α cells, and for recombinant protein expression in *E. coli* BL21 (DE3) cells. All PCR amplifications were carried out using Q5 High-Fidelity DNA Polymerase (New England Biosciences) and custom primers (IDT DNA) were used to introduce desired mutations. PCR products were designed with overlapping regions (at least 20 nucleotides) and used in Gibson assembly cloning (New England Biosciences) as per the manufacturer's guidelines. The BWG476 plasmid backbone was used for the *in vitro* transcription reaction, as described in the "*In vitro* Transcription of Luciferase mRNA" section.

Cryo-EM Sample Preparation and Data Collection

Purified 40S ribosomes were mixed with recombinantly purified MERS-CoV Nsp1 in a ratio of 1:10 and at a final concentration of 1.5 μM 40S ribosomal subunit. Complex formation was allowed to proceed for 30 min at 25°C. 4 μL of the MERS-CoV Nsp1:40S ribosomal subunit complex was applied to C-flat R2/1 holey carbon copper grids (EMS) after glow discharging the grids at 11 mA for 30 s (Pelco easiGlow, Ted Pella). Grids were blotted at blot force 1 for 6 s and plunge frozen in liquid ethane using the Vitrobot Mark IV system (ThermoFisher Scientific) maintained at 25°C. 0.05% CHAPSO (EMD Millipore) was used to ensure uniform ice thickness and particle distribution.

Grids were screened for optimal ice thickness and particle concentration. Data collection was done from a single screened grid using a 300 kV Titan Krios cryo-transmission electron microscope (ThermoFisher Scientific) equipped with a K3 camera (Gatan) and an imaging energy filter (Gatan) operated at a slit width of 15 eV. The dataset was collected in the counting super-resolution mode with a nominal magnification of 81,000x leading to a physical pixel size of 1.07 Å (super-resolution pixel size is 0.535 Å). The data were collected at a dose rate of 15 e^-/pixel/sec with a total electron dose of 50 $e^-/Å^2$ applied over 40 frames and a defocus range of −0.8 μm to −1.8 μm.

Cryo-EM data processing and model Building

The cryo-EM data processing workflow was done in cryoSPARC.[48] Frames were motion corrected using Patch motion correction and binned by a factor of 2 to yield 4043 micrographs. These micrographs were manually curated, and an initial round of particle picking was performed using Blob picker on a subset of 500 micrographs. A 2D classification job on these initial particle stack yielded

ideal 2D templates that were used to perform template-based particle picking on the entire dataset. A stack of 1,246,819 particles from template picker was subjected to 2D classification to weed out bad particles. After 2D classification, a select subset of 548,477 particles were carried forward to Ab initio and heterogeneous refinement. Particles corresponding to 40S ribosomal subunit classes were then pooled and subjected to 3D classification. One of the classes had a distinct density in the mRNA entry channel corresponding to the MERS-CoV Nsp1 and this stack of 267,551 particles was used for Non-uniform refinement to yield a reconstruction with a global resolution of 2.6 Å. This final particle stack (267,551 particles) belonging to the MERS-CoV Nsp1 bound 40S ribosome class were further processed using cryoSPARC's focused refinement job. The head and body regions of the consensus refinement reconstruction were masked, and the fulcrum coordinates were defined manually to yield better results from the focused refinement. The resulting reconstructions for the 40S head and body subvolumes showed significantly better map quality, especially in the flexible dynamic regions.

Model building was done in Coot[49] with a previously published model of human ribosome as the starting template (PDB 5A2Q). After initial rigid-body docking, the ribosomal RNA and protein residues were adjusted manually into the high-resolution map using real-space refinement modules. The CTD of MERS-CoV Nsp1 was built *de novo* into the high-resolution map. The focus refined maps were used to aid in model building of the dynamic regions of the 40S ribosomal subunit. Two rounds of real-space refinement in PHENIX[50] were carried out and the outliers were manually corrected in Coot before deposition in the Protein DataBank under the accession code '8T4S'.

Fluorescein-5-maleimide conjugation to Nsp1

SARS-CoV-2 Nsp1 and MERS Nsp1 constructs were engineered to have only one predicted solvent exposed cysteine residue. For the case of SARS-CoV-2 Nsp1, no endogenous cysteine residues were predicted to be solvent exposed. So, the following small extension was placed on the C terminus, GGSGGGGSGSC*. This construct was named Cys SARS2 Nsp1. For MERS-CoV Nsp1, two endogenous cysteines were predicted to be solvent exposed, C97 and C167. Cys167 was mutated to serine and this construct was named Cys MERS Nsp1. The two constructs were cloned and purified with the same procedure described in the *Bacterial Expression and Purification of Recombinant Nsp1 Proteins* section. The activity of the proteins was verified to be comparable to WT at 4μM Nsp1. Cys SARS2 Nsp1 (75 μM) was incubated for 30 min on ice in the presence of 2.5 M equivalents of Fluorescein-5-Maleimide (ThermoFisher Scientific) and 2 M equivalents of TCEP at a final pH of 7.4. Cys MERS Nsp1 (50 μM) was treated similarly, but with 11 M equivalents of Fluorescein-5-Maleimide and 3 M equivalents of TCEP. Both proteins were immediately purified post-labeling by size exclusion chromatography. Presence of unincorporated Fluorescein-5-Maleimide and protein concentration was determined by SDS-PAGE followed by whole gel fluorescence (excitation wavelength 495nm) and Coomassie staining band quantification, respectively. Band quantification was performed with dosimetric analysis against a non-conjugated Nsp1 control using ImageJ.[51]

Fluorescence polarization-based titrations

40S ribosomal subunit purified from rabbit reticulocytes (0–1000 nM) was titrated against 10 nM of either MERS-CoV or SARS-CoV-2 Cys Nsp1 protein and allowed to incubate at room temperature for 1 h. The fluorescence polarization of the reactions was measured using a fluorescence plate reader (Tecan, USA) at an excitation and emission wavelength of 495 nM and 515 nM, respectively. The titrations were carried out in triplicates and the standard deviation for each titration point was calculated. The curves were fit in Prism GraphPad (v9) to the following one-site binding equation –

$[Y = B_{max}*X/(K_d + X])$, wherein B_{max} is the maximum specific binding and K_d is the equilibrium dissociation constant.

QUANTIFICATION AND STATISTICAL ANALYSIS

Two-tailed, unpaired Student's T-tests were performed using Microsoft Excel to determine statistical significance in all *in-vitro* translation experiments. The exact statistical details can be found in figure legends 1A, 3B, and supplemental figure legend 1D. Briefly, technical replicates indicate experiments that were performed in parallel at the same time with the same reagent stocks. Three biological replicates were used for statistical testing. One biological replicate is shown along with the mean of three technical replicates. The standard deviation of the biological replicates is plotted in Figures 1A and 3B and the standard deviation of the technical replicates is plotted in Figure S1D. For the fluorescence polarization-based titrations, the standard deviation of the data from three technical replicates is plotted along with the binding curves. Exact details are provided in figure legend 1B.